

# Resonant Raman signatures of exciton polarons in a transition metal oxide: BiVO<sub>4</sub>

Georgy Gordeev,<sup>1</sup> Christina Hill,<sup>1,2</sup> Angelina Gudima,<sup>1</sup> Stephanie Reich,<sup>3</sup> and Mael Guennou<sup>1</sup>

<sup>1</sup>*Materials Research and Technology Department, University of Luxembourg, 41 rue du Brill, L-4422 Belvaux, Luxembourg*

<sup>2</sup>*Materials Research and Technology Department, Luxembourg Institute of Science and Technology, 41 rue du Brill, L-4422 Belvaux, Luxembourg*

<sup>3</sup>*Department of Physics, Freie Universität Berlin, Arnimallee 14, 14195 Berlin*

(Dated: April 8, 2024)

In this work we investigate the delocalized excitons and excitons trapped by a polaron formation in BiVO<sub>4</sub> by means of resonant Raman spectroscopy. We record Raman spectra with 16 laser lines between 1.9 and 2.6 eV and analyze intensity variations of the Raman peaks for different vibrational modes. The resonant Raman cross sections of the A<sub>g</sub> modes contain two types of resonances. The first high-energy resonance near 2.45 eV belongs to a transition between delocalized states; it is close to absorption edge measured at 2.3 eV and exhibits a characteristic 50 meV anisotropy between polarization parallel and perpendicular to the *c* axis. The high energy Raman resonance occurs inside the gap at 1.94 eV for all crystallographic directions. The in-gap resonance can involve a localized transition. We attribute it to an exciton-polaron, formed by a small localized electron polaron of Holstein type and delocalized holes. It manifests in the vibrations of vanadium and oxygen atoms where polaron localization occurs and the resonance energy matches theoretical predictions. The vibrational modes couple to the polaron with different efficiency determined from resonant Raman profiles.

Exciton polarons (EP) are quasiparticles that originate from an exciton trapped by its own lattice distortion field<sup>1-4</sup>. The excitons are charge neutral particles, yet their constituent electrons and holes can induce polaronic lattice distortions. EP can combine Fröhlich or Holstein electron-phonon coupling mechanisms with hydrogen-like excitonic wavefunction.<sup>4</sup> The exciton-polarons have been predicted in many materials, yet their clear experimental signatures are often elusive. EP might be responsible for the Stokes shift in direct band-gap semiconducting crystals,<sup>5</sup> where EP is referred to as self-trapped exciton<sup>6</sup>. This method only works in direct band gap semiconductors and other mechanisms can produce Stokes shifts in solids.<sup>7</sup> Further a softening of phonon replica in photoluminescence can be sign of EP, yet the phonons away from the  $\Gamma$  point can be at play.<sup>8</sup> There are reports of EPs in semiconducting 2D crystals, evidencing their nature by response to the doping, however they refer to a different phenomena where excitons couple to a Fermi sea and not lattice polarization.<sup>9</sup> A material system hosting polaronic and excitonic states is required to study EPs. Possible candidates could be transition metal oxides, such as TiO<sub>2</sub> and BiVO<sub>4</sub> can provide low screening required for high exciton binding energies<sup>10-12</sup> as well as light oxygen atoms favoring polaronic states.<sup>13-18</sup>

Resonant Raman spectroscopy has a potential to probe exciton-polaron states by leveraging enhanced polaron-phonon coupling. The Raman process always contains electron-phonon coupling term that can be enhanced when the energy of the incident or scattered radiation matches a real transition in a material.<sup>19</sup> Typical Raman resonances were achieved originate from band-to-band transitions<sup>20</sup> or many-body excitonic states<sup>21,22</sup>. More rare are the resonant Raman enhancement provided by the defect states<sup>23-25</sup> or Fermi level resonances<sup>26</sup>. EP states can be theoretically highlighted by resonant Raman spectroscopy given their intrinsically high electron phonon coupling. There are indication of EP enhanced Raman process in previous works, for instance a number of phonon overtones increases at the excitonic resonance, also new modes can appear<sup>27,28</sup> and intensity variation as function of doping may occur.<sup>29</sup> Yet these effects are indirect<sup>30</sup> and full resonant Raman profile is required containing both excitonic and EP resonances.

In this work, we implement resonant Raman scattering to study optical band gap and in gap transitions. We focus on EP states formed by small electron polarons in BiVO<sub>4</sub>. The signatures of these polarons manifest in the O-V tetrahedron modes with A<sub>g</sub> symmetry. These modes are excited with 16 excitation energies below and across the band gap. The Raman cross-section increases when excitation energy approaches either optical bands gap or transition involving polaronic state. By comparing the Raman cross section with direct optical absorption we can identify the excitonic bands gap transition at 2.45 eV and exciton-polaron energy at 1.94 eV. Using constant binding energies approximation we can directly determine the polaron hopping energies along different crystallographic axes.

We investigate symmetric A<sub>g</sub> modes that can couple to the same state twice and contain incoming and outgoing resonances. The A<sub>g</sub> modes Raman tensor contains small off-diagonal and large diagonal  $R_{jj}^{A_g}$  components, with  $j = a, b, c$ . The wavelength dependence of  $R_{jj}^{A_g}$  cross section can have contribution from delocalized excitons and localized exciton polarons. We restrict our analysis to only one EP and one exciton state for each  $j$  and total Raman scattering cross section is

$$R_{jj}^{A_g}(E_l) \propto E_l^4 |R_{jj}^{exc}(E_l) + R_{jj}^{EP}(E_l)|^2 \quad (1)$$

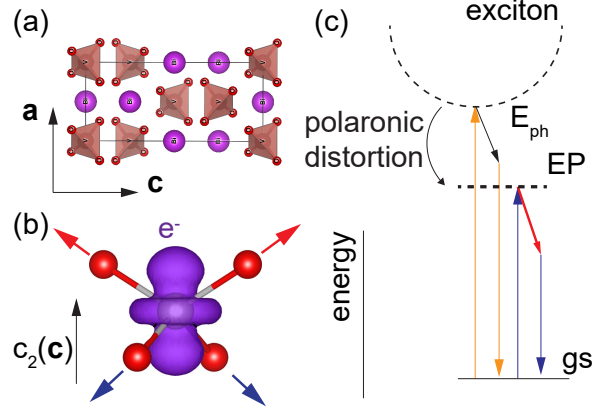


FIG. 1. Resonant Raman scattering by polarons, a) crystal structure of the monoclinic BiVO<sub>4</sub> with VO<sub>4</sub> tetrahedra faces highlighted. b) Spin density of the small Holstein polaron mode adapted from Pham and Deskins<sup>[13]</sup>, the arrows indicate the direction of the bands distortion. d) Scheme of a Resonant Raman scattering process via exciton and exciton-polaron (EP) band structure with Raman processes schematics. Vertical arrows are the photonic transitions, tilted arrows represent scattered phonons.

The excitonic contribution  $R_{jj}^{exc}$  is frequently described by the third-order perturbation theory yielding dependence on laser energy  $E_l$  as

$$R_{i,jj}^{Ag}(E_l) = \frac{M_{photon-i,jj}^2 M_{i-ph}}{(E_l - E_i^{jj} - i\gamma_i)(E_l - E_i^{jj} - E_{ph} - i\gamma_i)}. \quad (2)$$

For excitons  $i = exc$ , in the numerator we find the matrix element  $M_{photon-exc,jj}$  that represents the between exciton and a photon, and  $j$  indicates polarization of electric field oriented along  $a, b$  or  $c$  axis.  $M_{exc-ph}$  is the exciton-phonon matrix element.  $E_i^{jj}$  represents the energy of the exciton, that satisfies selection rule for  $j$  polarized electric field. This energy matches the  $E_{CB} - E_{VB} - E_B^{exc}$ , see schematic in Figure 1c.  $E_B$  is the binding energy of the exciton and  $E_{ph}$  is the energy of the phonon. The denominator contains so-called incoming and outgoing Raman resonances. The resonances are smeared together when excitonic broadening  $\gamma_i$  exceeds  $E_{ph}$ . In that case a maximum of the resonance is shifted to higher energy compared to  $E_i^{jj}$  by  $E_{ph}/2$ .

For calculating the contribution from EPs we use similar third-order perturbation theory approach as we used for excitons, but instead, the exciton-polaron serves as a basis of interactions with light and phonons. EP contribution to Raman cross section is given by Eq. (2), where  $i = EP$ . The EP resonant Raman process occurs in three steps, similar to excitonic process, where first EP is excited by a photon, then is scattered by a phonon and finally relaxes by emitting a Raman photon as shown in Figure 1c. However matrix elements and the energies are different, for instance  $E_{EP}$  in the case is  $E_{polaron} - E_{VB} - E_B^{EP}$ , where  $E_B^{EP}$  is the binding energy between localized electrons and delocalized holes. In the first approximation same value of  $E_B$  can be used for excitons and EPs. Further, in eq. (2) we use the  $M_{EP-phonon}$  matrix elements, that also reflect how much this phonon branch contributes to the EP formation. Thus resonant Raman cross-section contains detailed information about EP states.

Monoclinic bismuth vanadate (BiVO<sub>4</sub>) is a suitable playground to study polaron-enhanced Raman scattering. BiVO<sub>4</sub> is a well-established host of polaronic effects.<sup>13-18</sup> For example the Holstein polarons contribute to the anisotropic electrical conductivity and facilitates facet-selective charges accumulation.<sup>17,31</sup> The optical band gap of BiVO<sub>4</sub> is relatively low 2.3-2.4 eV, for example compared to other oxides hosting polaronic states as TiO<sub>2</sub> or HfO<sub>2</sub>. That makes sub-band and band gap excitation in BiVO<sub>4</sub> accessible by resonant Raman spectroscopy where setups typically work in the visible wavelength range. Further the BiVO<sub>4</sub> crystals carry signatures of coupled electron-hole states<sup>11</sup> with binding energies up to 0.6 eV.<sup>12</sup> Yet, theoretical description of BiVO<sub>4</sub> optical properties is incomplete. Most theoretical works report realistic optical band gap energies but systematically overestimate the anisotropy of the optical band gap by 0.5-0.6 meV.<sup>12,32,33</sup> Therefore a detailed study of anisotropic optical effects and specifically polaronic contribution is required. Resonant Raman spectroscopy would be an ideal tool reporting parameters both polaronic and excitonic transitions.

The crystal structure of BiVO<sub>4</sub> is shown in Figure 1a. Vanadium atoms are surrounded by oxygen tetrahedra. At room temperature BiVO<sub>4</sub> has a C2/c symmetry with lattice parameters (in the non-standard but more convenient I2/a setting)  $a = 5.186 \text{ \AA}$ ,  $b = 5.084 \text{ \AA}$ , and  $c = 11.69 \text{ \AA}$ ,  $\gamma = 89.61^\circ$ .<sup>34,35</sup> The small Holstein polarons are predicted

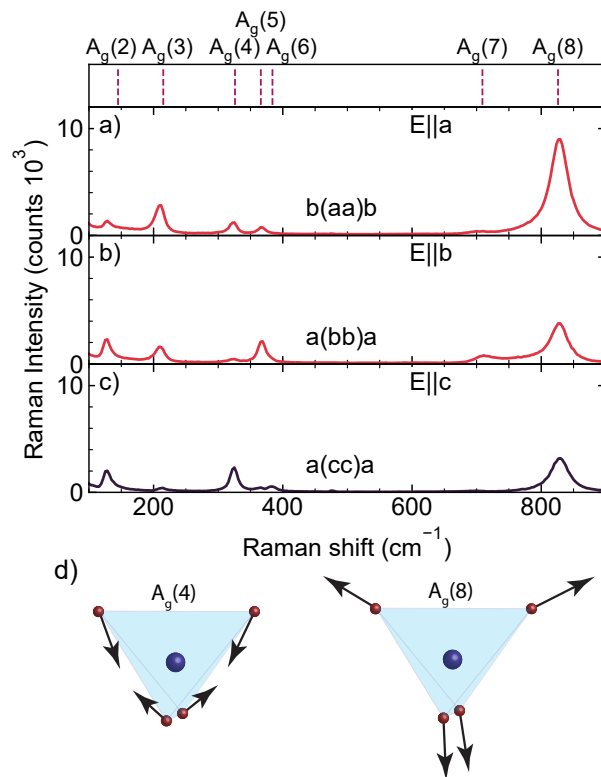


FIG. 2. Diagonal Raman tensor components  $R_{\alpha\alpha}$  of the  $A_g$  modes in the  $\text{BiVO}_4$  crystal. Raman spectra acquired with 2.3 eV excitation for incident and scattered photons polarized along a)  $E||a$ , b)  $E||b$ , and c)  $E||c$ . (d) Atom vibrations in a V-O tetrahedron: Eigenvectors of the  $A_g(8)$  mode and  $A_g(4)$  mode

to occur at the V-O tetrahedra. The excitonic transition originate from  $3d$  electrons in vanadium coupled to holes in oxygen from  $2p$  orbitals.<sup>12,32</sup> The polaronic wave function as calculated in Pham and Deskins<sup>[13]</sup> is depicted in Figure 1b, it is formed by the  $d_{z^2}$  electrons of vanadium and asymmetric stretching of the V-O bond, as schematically shown in Figure 1b. The polaronic state is localized and typically has a lower energy compared to the delocalized electron by  $2W_h$  where  $W_h$  is the polaron hopping energy, see Figure 1c. Both electron and polaron can couple to the valence band holes yielding a formation of excitonic and EP states, respectively, shown by dashed lines in Figure 1d. The energy difference between a hole-coupled and hole-uncoupled states is called exciton (EP) binding energy  $E_B$ .

We can now turn to the experimental analysis of the EP enhanced Raman scattering effects. For this purpose we used a single crystal purchased from SurfaceNet GmbH and grown by the Czochralski method. The Raman measurements were done on a Horiba T64000 microspectrometer with Rayleigh light rejected by long-pass filters and Raman signal dispersed by 900 grooves per mm grating. The laser light produced by a Coherent 70C Ar-Kr and Radiant Dye dye lasers. The spectral intensities are normalized by  $\text{CaF}_2$  reference, providing a constant Raman cross section in a visible wavelength range. We probe diagonal Raman tensor elements by using polarized Raman scattering. The mode decomposition yields in total 18 Raman active modes  $8A_g + 10B_g$ .<sup>36</sup> The high frequency  $A_g$  modes represent atom oscillations inside the  $\text{VO}_4$  tetrahedron. The  $A_g$  modes are scattered when the incident and scattered polarization are aligned. The modes excited with 2.3 eV laser in three different directions are shown in Figure 2. At this excitation energy the highest intensity is provided by the  $A_g(8)$  mode at  $\approx 826 \text{ cm}^{-1}$ . The highest diagonal component of  $A_g(8)$  is found for light polarized along the  $a$  direction  $b(aa)b$ , while  $A_g(4)$  mode at  $326 \text{ cm}^{-1}$  has the highest tensor component along  $b$ , see Figure 2a,b.

We further demonstrate excitation energy dependence of these modes. At first we study the  $a(cc)a$  scattering configuration. Two Raman spectra are exemplified in Figure 3a and b excited with 2.45 and 1.90 eV, respectively. The relative intensities of the  $A_g(8)$  and  $A_g(4)$  modes change drastically between the excitation lines. At 1.9 eV their amplitudes are almost equal, whereas at 2.45 eV the  $A_g(8)$  mode is dominating. Absolute Raman intensities vary as well. The Raman spectra measured with 16 laser energies from 1.87 to 2.71 eV are plotted after intensity calibration in a two-dimensional resonant Raman map in Figure 3c. On this map, the vertical axis represents the excitation

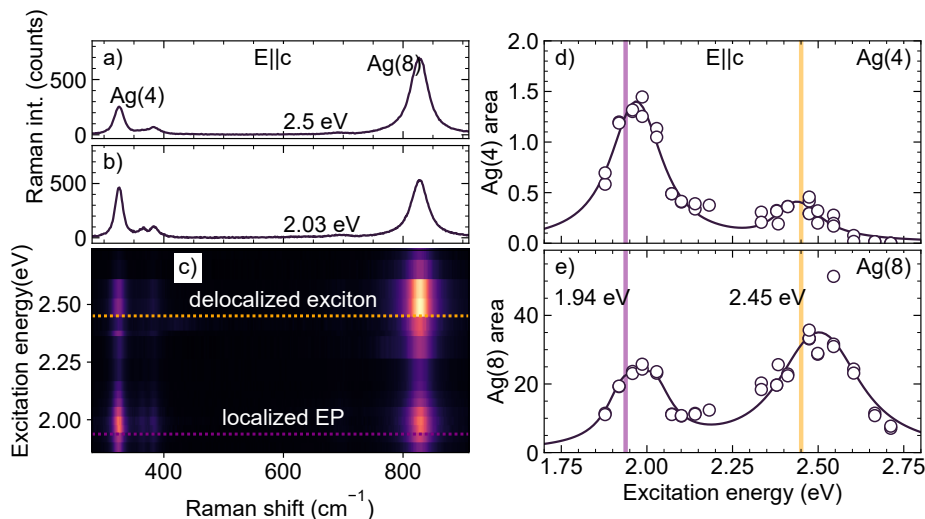


FIG. 3. Resonant Raman spectroscopy of the  $A_g$  modes with a(cc)a polarization. (a) Raman spectrum excited with 2.45 eV, near the band-gap energy, and (b) Raman spectrum excited below the band gap at 1.9 eV. (c) Resonant Raman map (d,e) Resonant Raman profile of the  $A_g(4)$  and  $A_g(8)$  modes, symbols represent experimental data and lines are fits by Eq. (2). Vertical lines represent the transition energies of the polaron and electron states, shifted from the transitions by  $E_{ph}/2$ .

energy and the horizontal axis the Raman shift while the color scales with Raman intensity. Two maxima can be clearly identified and are marked with horizontal lines in Figure 3c.

Using resonant Raman we can identify the energies the optical band gap transitions. The resonant Raman profile of the  $A_g(4)$  mode is shown in Figure 3d, where we plot the mode intensity obtained from a Lorentz fit as a function of excitation energy. The resonant Raman profile displays two resonances, same as the resonant Raman map (Figure 3c). We use eq. (1) for fitting the profiles. The fit results are shown by the solid lines in Figure 3d. From the fitting we extract the energies of two peaks 2.40 eV and 1.94 eV. The high energy resonance can be attributed to the optical band gap transition, it is close to the previously reported absorption band edge<sup>33,37</sup> and band edge we later estimate from Tauc plots. Resonant Raman directly cannot verify the excitonic character of the resonance, however based on previous works the absorption edge originates from an excitonic state with binding energies between 0.4-0.6 eV.<sup>11,12</sup>

We attribute Raman resonance at 1.94 eV to exciton-polaron, formed by localized electrons and delocalized holes. This state is localized  $\approx 0.5$  eV deep inside the gap by assuming similar  $E_B^{exc}$  and  $E_B^{EP}$ . This large energy below the gap is characteristic for small highly electron-polarons.<sup>13</sup> Less likely this can be a hole based EP, where localized holes couple to the delocalized electrons. The hole polarons in monoclinic  $\text{BiVO}_4$  are larger compared to the unit cell and their energy is predicted to be only 150 meV higher than valence band,<sup>15</sup> which doesn't agree well with our experiment. The defect states can also create additional real states inside the gap, however in the case of  $\text{BiVO}_4$  some of them directly yield access charge carriers and promote polarons formation. In the other cases the bound states energies 0.5-1 eV below the band gap,<sup>38,39</sup> that can for example manifest in the photoluminescence (PL) at lower energies attributed to oxygen vacancies. However the broadening of the defect bound states is quite large 0.5 eV,<sup>40</sup> indicating their short lifetimes that are not compatible with we obtain from the resonant Raman profile. Based on the in gap state at 1.94 eV energy and broadening of 85 meV the Raman in gap resonance from Figure 3c we attribute to the EP states. The polaronic character of this transition can be further corroborated by studying its peculiar coupling to phonons in more detail.

We probe EP-phonon coupling by comparing the resonant Raman profiles of different vibrational modes. The intensity distribution between excitonic and EP Raman resonances is different for the  $A_g(4)$  and  $A_g(8)$  modes. The  $A_g(4)$  mode couples more strongly to the EP transition at 1.95 eV. On the other hand,  $A_g(8)$  couples more strongly to the excitonic band gap transition at 2.45 eV. The matrix elements  $M_{ex-phonon}$  and  $M_{EP-phonon}$  depend on the vibration type, while both modes have the same  $A_g$  symmetry in the complete unit cell of  $\text{BiVO}_4$ , they have different local behavior within V-O tetrahedron where polaron wavefunction is localized. Within  $\text{VO}_4$  tetrahedron the  $A_g(8)$  mode appear to fully symmetric non-polar, see Figure 1g. All four oxygen atoms move towards vanadium atom performing breathing-like vibration, symmetrically stretching the V-O bonds. On the other hand the  $A_g(4)$  mode has a bending-like character, with two top and bottom oxygen atoms moving upwards and downwards simultaneously, see

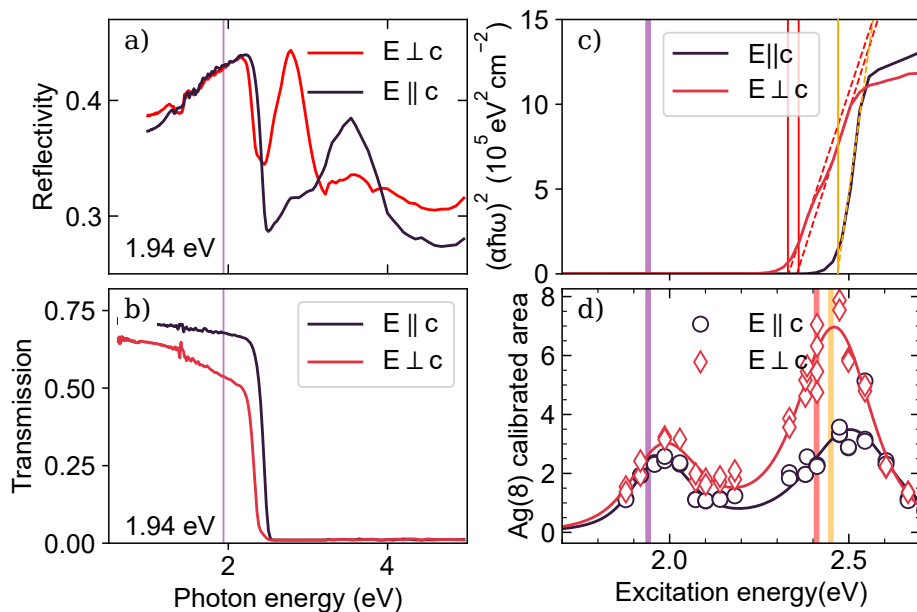


FIG. 4. Band gap anisotropy of the  $\text{BiVO}_4$  crystal. a) Optical reflectivity spectra for  $E||a,b$  and for  $E||c$ . b) Optical transmission spectra. c) Tauc plots at the energies of exciton and EP. d) Resonant Raman profiles of the  $A_g(8)$  mode with laser light polarized along  $c$  and  $b$  crystallographic axes. In c) and d) the vertical purple line marks the position of the EP state.

eigenvectors in Figure 3f. Both modes contain  $C_2(z)$  operation, compatible with the polaron wavefunction, yet the  $A_g(4)$  appears to couple more strongly to the polaron compared to the delocalized electron.

We now measure the linear optical properties of  $\text{BiVO}_4$  to disentangle the contributions from the EP and exciton states. The optical spectra were measured in 5 nm step with light polarized parallel and perpendicular to the  $c$  axis using a Lambda 1050+ uv/vis/nir Perkin-Elmer spectrometer, see Figure 4c. Anisotropy in the lowest optical band gap energies visible both in transmission and reflectivity spectra, shown in Figure 4a,b. We quantify the optical band gaps using Tauc plots shown in Figure 4c, where  $(\alpha\hbar\omega)^n$  is plotted versus  $\hbar\omega$ . The absorption coefficient  $\alpha$  is calculated as  $\frac{1}{d}\log(\frac{1-R}{T})$ . For fitting the Tauc plots we choose  $n = 2$  most appropriate for crystalline materials.<sup>41</sup> The linear fit yields single energy for  $E_{exc}^c = 2.47$  eV and two energies for  $E \perp c$ ,  $E_{exc}^{a,b} = 2.33$  and 2.37 eV, that correspond to  $a$  and  $b$  domains. These high energy states manifest themselves in regular way both in optical absorption and resonant Raman, thus we confirm that the high energy Raman resonance belongs to the excitonic state.

The EP state can introduce the band edge asymmetry near the excitonic absorption. At first glance we find no optical features at at 1.94 eV in transmission and reflectivity spectra, see purple line in Figure 4a,b. However a closer look at the absorption edge reveals an anomaly in symmetry of the absorption band-edge. The asymmetry of the dielectric function can be a sign of EP polaronic states.<sup>42</sup> This is visible by the shape of Reflectivity spectra near 2.3 eV the reflectivity drops down without increasing first. We show how the asymmetry of absorption peak changes the shape of dielectric function in Supplementary Figure 1, where we adapt a Fano line-shape as a real part of dielectric function. The fit results are shown in Supplementary Figure 2c. We used symmetric Lorentz oscillators for higher energy peaks and Fano line shape for the lowest energy resonance. Thus EP states below the band gap can make the optical absorption edge asymmetric.

With resonant Raman we can further probe optical anisotropy of the EP and excitonic states. It is achieved by comparing resonant Raman profiles of the *same modes* excited in varying polarization conditions. Figure 4d compares the resonant Raman profiles of the  $A_g(8)$  mode with the electric field polarized along the  $c$  and along the  $b$  axis. The high-energy resonance occurs at different energies, for the  $a(cc)a$  configuration the  $E_{exc} = 2.41$  eV, whereas for the  $c(aa)c$  we find the  $E_{exc}$  at 2.45 eV. The total anisotropy reported by resonant Raman is 40 meV. The anisotropy is of the same magnitude as reported by optical spectroscopy; however, the reflectivity analysis overestimates it by  $\approx 50$  meV, compared to resonant Raman analysis, see Figure 4d. The divergence of the resonant Raman from optical analysis we attribute to the EP tail, discussed in the previous paragraph. Resonant Raman spectroscopy is more accurate in that regard as it clearly separates EP and excitonic processes and can report their energies precisely.

We can determine the polaron parameters using resonant Raman profiles. When the Holstein polaron is hopping

along the crystal axis it must overcome the energy of the local potential well  $W_h$ .<sup>43</sup> For  $W_h$  estimation we approximate the binding energies of exciton and EP to be the same. In all three crystallographic directions we find the same EP energy  $E_{pol}$  1.94 eV, see vertical blue line in Figure 4e,f. The polaron hopping energy can be determined as  $W_h = (E_{CB} - E_{polaron})/2 = (E_{EP} - E_{exc})/2$ . For the  $c$  axis we find  $W_h^c = 255$  meV, whereas for the  $a,b$  axes we find  $W_h^{a,b} = 235$  meV. This values can be directly compared to the first-principles calculations to determine the Hubbard energy. We can now compare the polaron energy with theoretical DFT+U calculations. By variation the Hubbard energy  $U$  different values of in-gap polaronic state are possible. The experimental hopping energies correspond to  $U \approx 2$  eV.<sup>13</sup> This agrees well with BiVO<sub>4</sub> polarons stability criterion, when  $U$  must be more 2 eV for polarons to form.<sup>13</sup>

In summary, we demonstrated that exciton-polarons can contribute to the resonant Raman cross section along with excitonic transitions. We measured the resonant Raman profiles of the A<sub>g</sub> modes in BiVO<sub>4</sub> in two crystallographic directions. Raman profiles show two types of resonances. The first resonance at 2.41-2.45 eV near the optical band gap energy and second, inside the band gap at 1.9 eV. The first resonance is attributed to the delocalized excitonic transition, it is visible in reflectivity spectra and displays 50 meV anisotropy. We attribute the second resonance to the EP transition. The strength of that resonance is proportional to the polaron-phonon and polaron-photon coupling, which we confirm by analyzing different phonons excited in three different polarization conditions. This demonstrates that resonant Raman is a precise tool to analyze signatures of exciton-polarons in oxide materials and can report their parameters with high precision of optical spectroscopies. EP induced Raman enhancement has high potential for future experimental and theoretical studies of exciton-polarons and bare polarons, where excitonic effect is not always necessary for Raman enhancement to occur. Further the polaron enhancement process can be applied to other polaron types, for instance large hole-type polaron can be formed around bismuth atom in BiVO<sub>4</sub>. The corresponding signatures would be contained in the B<sub>g</sub> modes that mostly involve Bi-O vibrations at the energies closer to the optical band gap. In addition, the defect bound<sup>44</sup> and spin polaron<sup>45</sup> states could be examined in other materials. Another field of study of polaron enhanced Raman scattering could be surface polaronic states. In addition surface polarons may yield co-called "shake-off" signatures<sup>46</sup> with a series of Raman resonances, separated by phonon energy. Thus we show that resonant Raman spectroscopy is an excellent tool with high potential to study exciton-polarons in semiconducting crystals that can directly report their energies.

## ACKNOWLEDGMENTS

GG, MG, and CH acknowledge funding from the Fond National de la Recherche under Project PRIDE/15/10935404. This research was funded in whole, or in part, by the Luxembourg National Research Fund (FNR), grant reference [INTER/MERA20/14995416/SWIPE/AWORD]. For the purpose of open access, and in fulfilment of the obligations arising from the grant agreement, the author has applied a Creative Commons Attribution 4.0 International (CC BY 4.0) license to any Author Accepted Manuscript version arising from this submission. The authors are grateful to J. Iniguez, H-J Zhao, D. Vincent and X. Rocquefelte for preliminary calculations of BiVO<sub>4</sub> phonon modes and eigenvectors.

- 
- [1] G. Iadonisi and F. Bassani, Excitonic polaron states and optical transitions, *Il Nuovo Cimento D* **2**, 1541 (1983).
  - [2] Y. Toyozawa and J. Hermanson, Exciton-phonon bound state: A new quasiparticle, *Physical Review Letters* **21**, 1637 (1968).
  - [3] Z. Dai, C. Lian, J. Lafuente-Bartolome, and F. Giustino, Excitonic polarons and self-trapped excitons from first-principles exciton-phonon couplings, *Physical Review Letters* **132**, 036902 (2024).
  - [4] Z. Dai, C. Lian, J. Lafuente-Bartolome, and F. Giustino, Theory of excitonic polarons: From models to first-principles calculations, *Physical Review B* **109**, 045202 (2024).
  - [5] J. Li, H. Wang, and D. Li, Self-trapped excitons in two-dimensional perovskites, *Frontiers of Optoelectronics* **13**, 225 (2020).
  - [6] R. Williams and K. Song, The self-trapped exciton, *Journal of Physics and Chemistry of Solids* **51**, 679 (1990).
  - [7] F. Yang, M. Wilkinson, E. J. Austin, and K. P. O'Donnell, Origin of the stokes shift: A geometrical model of exciton spectra in 2d semiconductors, *Physical Review Letters* **70**, 323 (1993).
  - [8] H.-C. Hsu and W.-F. Hsieh, Excitonic polaron and phonon assisted photoluminescence of zno nanowires, *Solid State Communications* **131**, 371 (2004).

- [9] A. J. Campbell, M. Brotons-Gisbert, H. Baek, V. Vitale, T. Taniguchi, K. Watanabe, J. Lischner, and B. D. Gerardot, Exciton-polarons in the presence of strongly correlated electronic states in a moiré superlattice, *npj 2D Materials and Applications* **6**, 79 (2022).
- [10] E. Baldini, L. Chiodo, A. Dominguez, M. Palumbo, S. Moser, M. Yazdi-Rizi, G. Auböck, B. Mallett, H. Berger, A. Margrez, C. Bernhard, M. Grioni, A. Rubio, and M. Chergui, Strongly bound excitons in anatase  $\text{TiO}_2$  single crystals and nanoparticles, *Nature Communications* **8**, 13 (2017).
- [11] J. Zhang, J. Shi, Y. Chen, K. H. Zhang, and Y. Yang, Bimolecular self-trapped exciton formation in bismuth vanadate, *Journal of Physical Chemistry Letters* **13**, 9815 (2022).
- [12] T. Das, X. Rocquefelte, R. Laskowski, L. Lajaunie, S. Jobic, P. Blaha, and K. Schwarz, Investigation of the optical and excitonic properties of the visible light-driven photocatalytic  $\text{BiVO}_4$  material, *Chemistry of Materials* **29**, 3380 (2017).
- [13] T. D. Pham and N. A. Deskins, Efficient method for modeling polarons using electronic structure methods, *Journal of Chemical Theory and Computation* **16**, 5264 (2020).
- [14] K. E. Kweon, G. S. Hwang, J. Kim, S. Kim, and S. Kim, Electron small polarons and their transport in bismuth vanadate: A first principles study, *Physical Chemistry Chemical Physics* **17**, 256 (2015).
- [15] K. E. Kweon and G. S. Hwang, Structural phase-dependent hole localization and transport in bismuth vanadate, *Physical Review B - Condensed Matter and Materials Physics* **87**, 10.1103/PhysRevB.87.205202 (2013).
- [16] T. Liu, Q. Zhao, C. Li, Y. Lyu, and M. Dupuis, Photocatalytic facet selectivity in  $\text{BiVO}_4$  nanoparticles: Polaron electronic structure and thermodynamic stability considerations for photocatalysis, *Journal of Physical Chemistry C* **123**, 20142 (2019).
- [17] T. Liu, X. Zhou, M. Dupuis, and C. Li, The nature of photogenerated charge separation among different crystal facets of  $\text{BiVO}_4$  studied by density functional theory, *Physical Chemistry Chemical Physics* **17**, 23503 (2015).
- [18] J. Wiktor, F. Ambrosio, and A. Pasquarello, Role of polarons in water splitting: The case of  $\text{BiVO}_4$ , *ACS Energy Letters* **3**, 1693 (2018).
- [19] P. Y. Yu and M. Cardona, *Fundamentals of Semiconductors – Physics and Materials Properties* (Springer, Berlin Heidelberg, 1995) pp. 18–83, arXiv:arXiv:1011.1669v3.
- [20] J. B. Renucci, R. N. Tyte, and M. Cardona, Resonant raman scattering in silicon, *Physical Review B* **11**, 3885 (1975).
- [21] G. Gordeev, A. Jorio, P. Kusch, B. G. Vieira, B. Flavel, R. Krupke, E. B. Barros, and S. Reich, Resonant anti-stokes raman scattering in single-walled carbon nanotubes, *Physical Review B* **96**, 245415 (2017).
- [22] Spectroscopy of excited yellow exciton states in  $\text{Cu}_2\text{O}$  by forbidden resonant raman scattering, *Physical Review B* **15**, 2145 (1977).
- [23] M. C. Weber, M. Guennou, C. Toulouse, M. Cazayous, Y. Gillet, X. Gonze, and J. Kreisel, Temperature evolution of the band gap in  $\text{BiFeO}_3$  traced by resonant raman scattering, *Physical Review B* **93**, 10.1103/PhysRevB.93.125204 (2016).
- [24] V. N. Popov, L. Henrard, and P. Lambin, Resonant raman spectra of graphene with point defects, *Carbon* **47**, 2448 (2009).
- [25] A. K. Arora and A. K. Ramdas, Resonance raman scattering from defects in  $\text{CdSe}$ , *Physical Review B* **35**, 4345 (1987).
- [26] J. P. Bonacum, A. O'Hara, D.-L. Bao, O. S. Ovchinnikov, Y.-F. Zhang, G. Gordeev, S. Arora, S. Reich, J.-C. Idrobo, R. F. Haglund, S. T. Pantelides, and K. I. Bolotin, Atomic-resolution visualization and doping effects of complex structures in intercalated bilayer graphene, *Physical Review Materials* **3**, 064004 (2019).
- [27] B. Mihailova, G. D. Ventura, N. Waesermann, W. Xu, J. Schlüter, F. Galdenzi, A. Marcelli, G. J. Redhammer, M. Boiocchi, and R. Oberti, Atomistic insight into lithospheric conductivity revealed by phonon–electron excitations in hydrous iron-bearing silicates, *Communications Materials* **2**, 10.1038/s43246-021-00161-y (2021).
- [28] B. Mihailova, G. D. Ventura, N. Waesermann, S. Bernardini, W. Xu, and A. Marcelli, Polarons in rock-forming minerals: Physical implications, *Condensed Matter* **7**, 10.3390/condmat7040068 (2022).
- [29] M. Bartonek and H. Kuzmany, Resonance raman scattering from the polaron state in polyaniline (1991).
- [30] C. Ulrich, A. Gössling, M. Grüniger, M. Guennou, H. Roth, M. Cwik, T. Lorenz, G. Khaliullin, and B. Keimer, Raman scattering in the mott insulators  $\text{LaTiO}_3$  and  $\text{YTiO}_3$ : Evidence for orbital excitations, *Physical Review Letters* **97**, 10.1103/PhysRevLett.97.157401 (2006).
- [31] R. Li, F. Zhang, D. Wang, J. Yang, M. Li, J. Zhu, X. Zhou, H. Han, and C. Li, Spatial separation of photogenerated electrons and holes among  $\{010\}$  and  $\{110\}$  crystal facets of  $\text{BiVO}_4$ , *Nature Communications* **4**, 10.1038/ncomms2401 (2013).
- [32] Z. Zhao, Z. Li, and Z. Zou, Electronic structure and optical properties of monoclinic clinobisvanite  $\text{BiVO}_4$ , *Physical Chemistry Chemical Physics* **13**, 4746 (2011).
- [33] C. Hill, M. C. Weber, J. Lehmann, T. Leinen, M. Fiebig, J. Kreisel, and M. Guennou, Role of the ferroelastic strain in the optical absorption of  $\text{BiVO}_4$ , *APL Materials* **8**, 10.1063/5.0011507 (2020).
- [34] R. S. Roth and J. L. Waring, Synthesis and stability of bismutotantalite, stibiotantalite and chemically similar  $\text{ABO}_4$  compounds, *American Mineralogist* **48**, 1348 (1963).
- [35] S. H. Choh and M. S. Jang, Domain structure and magnetic resonance studies of ferroelastic  $\text{BiVO}_4$  revisited, *Materials Research Express* **3**, 045021 (2016).
- [36] J. Pellicer-Porres, D. Vázquez-Socorro, S. López-Moreno, A. Muñoz, P. Rodríguez-Hernández, D. Martínez-García, S. N. Achary, A. J. Rettie, and C. B. Mullins, Phase transition systematics in  $\text{BiVO}_4$  by means of high-pressure-high-temperature raman experiments, *Physical Review B* **98**, 1 (2018).
- [37] S. Tokunaga, H. Kato, and A. Kudo, Selective preparation of monoclinic and tetragonal  $\text{BiVO}_4$  with scheelite structure and their photocatalytic properties, *Chemistry of Materials* **13**, 4624 (2001).

- [38] N. Österbacka, F. Ambrosio, and J. Wiktor, Charge localization in defective bivo 4, *The Journal of Physical Chemistry C* **126**, 2960 (2022).
- [39] N. Österbacka and J. Wiktor, Influence of oxygen vacancies on the structure of bivo 4, *The Journal of Physical Chemistry C* **125**, 1200 (2021).
- [40] J. K. Cooper, S. B. Scott, Y. Ling, J. Yang, S. Hao, Y. Li, F. M. Toma, M. Stutzmann, K. V. Lakshmi, and I. D. Sharp, Role of hydrogen in defining the n-type character of bivo 4 photoanodes, *Chemistry of Materials* **28**, 5761 (2016).
- [41] J. Klein, L. Kampermann, B. Mockenhaupt, M. Behrens, J. Strunk, and G. Bacher, Limitations of the tauc plot method, *Advanced Functional Materials* **33**, 10.1002/adfm.202304523 (2023).
- [42] X. Chi, L. Mandal, C. Liu, A. D. Fauzi, A. Chaudhuri, T. J. Whitcher, H. K. Jani, Z. Chen, S. Xi, C. Diao, M. A. Naradipa, X. Yu, P. Yang, A. H. Castro-Neto, M. B. Breese, K. P. Loh, T. V. Venkatesan, and A. Rusydi, Unravelling a new many-body large-hole polaron in a transition metal oxide that promotes high photocatalytic activity, *NPG Asia Materials* **14**, 10.1038/s41427-022-00364-w (2022).
- [43] Y. Natanzon, A. Azulay, and Y. Amouyal, Evaluation of polaron transport in solids from first-principles, *Israel Journal of Chemistry* **60**, 768 (2020).
- [44] M. Setvin, C. Franchini, X. Hao, M. Schmid, A. Janotti, M. Kaltak, C. G. V. de Walle, G. Kresse, and U. Diebold, Direct view at excess electrons in tio 2 rutile and anatase, *Physical Review Letters* **113**, 086402 (2014).
- [45] H. Y. Huang, Z. Y. Chen, R. P. Wang, F. M. F. de Groot, W. B. Wu, J. Okamoto, A. Chainani, A. Singh, Z. Y. Li, J. S. Zhou, H. T. Jeng, G. Y. Guo, J.-G. Park, L. H. Tjeng, C. T. Chen, and D. J. Huang, Jahn-teller distortion driven magnetic polarons in magnetite, *Nature Communications* **8**, 15929 (2017).
- [46] M. Kang, S. W. Jung, W. J. Shin, Y. Sohn, S. H. Ryu, T. K. Kim, M. Hoesch, and K. S. Kim, Holstein polaron in a valley-degenerate two-dimensional semiconductor, *Nature Materials* **17**, 676 (2018).

# Supporting information: Resonant Raman signatures of electron polarons in monoclinic bismuth vanadate

Georgy Gordeev,<sup>1</sup> Christina Hill,<sup>1,2</sup> Angelina Gudima,<sup>1</sup> Stephanie Reich,<sup>3</sup> and Mael Guennou<sup>1</sup>

<sup>1</sup>*University of Luxembourg, 41 rue du Brill, L-4422 Belvaux, Luxembourg*

<sup>2</sup>*Materials Research and Technology Department, Luxembourg Institute of Science and Technology, 41 rue du Brill, L-4422 Belvaux, Luxembourg*

<sup>3</sup>*Freie Universität Berlin, Department of Physics, Arnimallee 14, 14195 Berlin*

(Dated: April 8, 2024)

## REFLECTIVITY FITTING USING KRAMERS-KRONIG RESTRICTIONS

A symmetric optical resonance can be represented by a Lorentz peak:

$$Lor(\omega) = \frac{4g^2}{\omega^2 - \omega_0^2 - i\gamma\omega}, \quad (1)$$

with  $g$  equal to light-matter coupling strength,  $\omega_0$  resonant frequency, and  $\gamma$  electronic broadening. Eq. (1) automatically follows the Kramers-Kronig (KK) transformation rules relating the imaginary and real components of dielectric function. The summ of Lorentz resonances is typically used for describing electronic resonances in the dielectric function. However Eq. (1) is not suitable when the resonance is asymmetric.

The lowest energy transition in  $\text{BiVO}_4$  is asymmetric due to the polaronic band edge inside the gap. In order to describe the polaron altered dielectric function we produce a complex Fano-based line shape using the KK transformation. We start from an imaginary component of  $\epsilon$ , where we use an asymmetric Fano peak:

$$Fano''(\omega) = \frac{g \cdot \left(1 + \frac{\omega - \omega_0}{y/2} \cdot as\right)^2}{1 + \left(\frac{\omega - \omega_0}{y/2}\right)^2}, \quad (2)$$

where  $y$  stands for fwhm,  $\omega_0$  for resonance position, and  $g$  is proportional to the oscillator strength. The  $as$  parameter represents peak asymmetry. The dielectric function obeys the KK transformation:

$$Fano'(\omega) = \frac{2}{\pi} \int_0^\infty \frac{\omega_2 Fano''(\omega_2) - \omega Fano''(\omega)}{\omega_2^2 - \omega^2} \delta\omega_2 \quad (3)$$

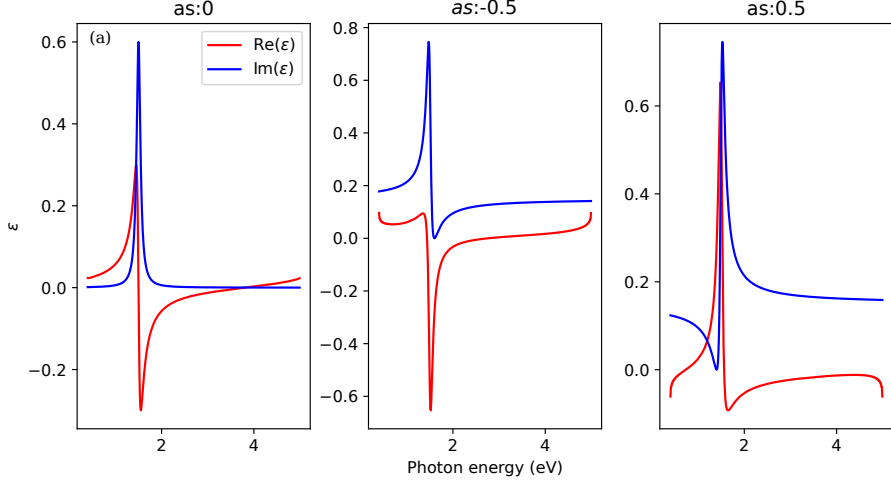


FIG. 1. Asymmetric Fano peak calculated by eq. (4) with different  $as$  parameters. Fully symmetric in (a) with  $as = 0$ , negative asymmetry in (b) with  $as = -0.5$ , and positive asymmetry in (c)  $as = 0.5$

We will use a similar expression rules we can recover the complex peak shape from the Hilbert space transformation:

$$Fano(\omega) = Fano'(\omega) + i \cdot Fano''(\omega) = F^{-1}(Fano''(\omega)2U), \quad (4)$$

where  $F$  is the Fourier transform and  $U$  is the unitary transform. Figure 1 examples the real and imaginary components of the dielectric function of the Fano peak for different gedrees of asymmetry  $as$ .

For fitting the experimental reflectivity spectra we implement the dielectric function represented by one Fano oscillator and a series of Lorenz oscillators:

$$\epsilon(\omega) = e_b \cdot (1 + Fano(\omega) + \sum_i Lor_i(\omega)), \quad (5)$$

where  $e_b$  is the background dielectric function.

The reflectivity at normal incidence is calculated with Frensel equation

$$R(\omega) = \left| \frac{n_{air} - n_{BVO}(\omega)}{n_{air} + n_{BVO}(\omega)} \right|^2. \quad (6)$$

Refractive index of air  $n_{air} = 1$  and refractive index of  $BiVO_4$   $n_{BVO}$  is calculated from dielectric functon.

$$n_{BVO}(\omega) = \sqrt{\epsilon(\omega)}. \quad (7)$$

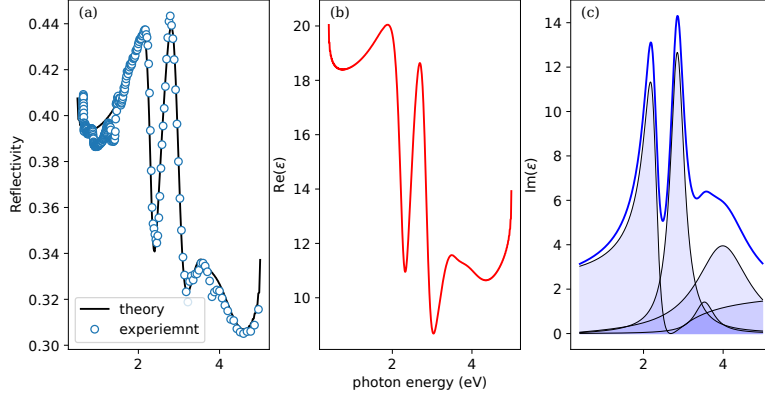


FIG. 2. Reflectivity analysis of the  $\text{BiVO}_4$  sample with light polarized perpendicular to  $c$ . (a) Reflectivity spectrum, symbols represent experimental data and lines fits with Eqs. (6) and (5). (b) The real and (c) imaginary components of the dielectric function.

Now we show the fit results for EM field oriented along  $c$  and along  $a,b$ . The experimental reflectivity spectrum is shown in Figure 2a for light polarized along  $X$  direction. The experimental data are represented by the symbols and the lines are fits by eqs. (6) and (5). The real and imaginary components of the dielectric function are plotted in Figure 2b, and c. Each of the resonance is highlighted in the imaginary part of the plot. The lowest energy peak represent the band-gap transition merged with a polaron. The total line shape is asymmetric with tail extending into the infra-red.

Now we investigate other dielectric tensor components. Figure 3a shows the experimental reflectivity spectrum for light polarized along  $a,b$ . We cannot distinguish between  $a$  and  $b$  since our white beam is much larger than the domain size. In similar manner we fit the reflectivity spectra by a set of optical resonances. The fit results are shown in Figure 3a by lines. From the fit we recover  $Im(\epsilon)$  and  $Re(\epsilon)$  shown in Figure 3b,c.

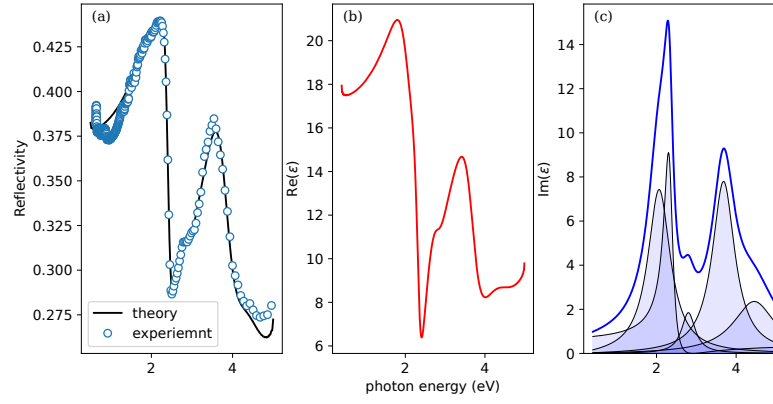


FIG. 3. Reflectivity analysis of the  $\text{BiVO}_4$  sample with light polarized along  $c$ . (a) Reflectivity spectrum, symbols represent experimental data and lines fits with Eqs. (6) and (5). (b) The real and (c) imaginary components of the dielectric function.